

Computer Tomography on Divertor Impurity Monitor for ITER with Minimizing Errors in a Logarithmic Scale^{*)}

Hiroki NATSUME, Shin KAJITA¹⁾, Vladislav S. NEVEROV²⁾, Radmir I. KHUSNUTDINOV^{2,3)}, Evgeny VESHCHEV⁴⁾, Maarten DE BOCK⁴⁾, Alexei R. POLEVOI⁴⁾, Hirohiko TANAKA, Noriyasu OHNO, Hiroaki OGAWA⁵⁾ and Sin-iti KITAZAWA⁵⁾

Graduate School of Engineering, Nagoya University, Nagoya 464-8603, Japan

¹⁾*Institute of Materials and Systems for Sustainability, Nagoya University, Nagoya 464-8603, Japan*

²⁾*NRC Kurchatov Institute, Kurchatov sq. 1, 123182 Moscow, Russian Federation*

³⁾*NRNU MEPhI, Kashirskoye sh. 31, 115409 Moscow, Russian Federation*

⁴⁾*ITER Organization, 13115 St. Paul-lez-Durance, France*

⁵⁾*Naka Fusion Institute, National Institutes for Quantum and Radiological Science and Technology (QST), Naka 311-0193, Japan*

(Received 13 November 2020 / Accepted 6 January 2021)

The computer tomography for divertor impurity monitor, which measures plasma emissions in the divertor region, for ITER has been conducted using a ray-tracing technique. We have attempted four different solution methods for the inversion problem and compared the results. The solution methods which minimize errors in logarithmic scale had better performance than the methods which minimize errors in linear scale. This is likely due to the fact that the values in the emission profile vary in a wide range of orders of magnitude. The accuracy of the reconstruction has been investigated by changing discharge conditions and the number of field-of-views used. The deterioration in accuracy was most noticeable when the emission profile was reconstructed using only two field-of-views. In addition, the accuracy deteriorated, making the estimation more challenging, under discharge conditions with low emission intensity because of the wider range of emission intensity under such conditions.

© 2021 The Japan Society of Plasma Science and Nuclear Fusion Research

Keywords: divertor impurity monitor, computer tomography, ray-tracing, inversion problem, tokamak diagnostic

DOI: 10.1585/pfr.16.2405019

1. Introduction

Divertor impurity monitor (DIM) has been developed to achieve the required specifications for the ITER plasma measurement [1–5]. The DIM consists of six field-of-views (FOVs) and measures plasma emissions in the wavelength range of 200 to 1000 nm in the divertor region. The expected impurities are those originating from the first wall and divertor target and gases injected into the divertor plasma for radiation cooling. The main functions of this system are to measure the two-dimensional distribution of concentrations and influxes of impurities, deuterium, and tritium in the divertor region and to identify the ionization front position [6].

Stray light produced by reflection on the first wall and divertor is one of the major issues in spectroscopic diagnostics including DIM. Since tungsten, which has a high optical reflectance, is used for divertor material, the measured signals are jeopardized to be contaminated by the reflected light on the divertor surface [7]. Therefore, it is important for accurate measurements to consider the reflection effects, and one option is to evaluate quantitatively the

reflected light based on reflection modeling [8]. In recent studies, a ray-tracing approach, which enables to assess the light reflection, has been studied and developed [9–12]. In a tomography process, the use of ray-tracing results considering the reflection effect can mitigate an overestimation and remove artifacts in a reconstructed emission [11]. Further, applications of the tomographic approach to the spectroscopic measurement signals were reported to extract the direct light without reflections [12, 13].

In this study, we used the ray-tracing framework Raysect [14] and the spectroscopy modeling framework CHERAB [15] to simulate the incident light of D_α (656.1 nm) emission on the DIM including the reflected light. In addition, we reconstructed two-dimensional emission profiles in the divertor region from the measured signals on the DIM and compared them with respect to tomography methods, number of FOVs used in tomography, and discharge conditions. Also, we propose a new solution method that introduces error minimization in logarithmic scale to simultaneous iterative reconstruction technique (L-SIRT). From the comparison of tomography methods, the proposed method showed better performance than the methods that minimize errors in linear scale. This is likely

author's e-mail: natsume.hiroki@d.mbox.nagoya-u.ac.jp

^{*)} This article is based on the presentation at the 29th International Toki Conference on Plasma and Fusion Research (ITC29).

due to the fact that the values in the emission profile vary in a wide range of orders of magnitude. The ray-tracing setup and computer tomography methods will be given in the following section. The results and evaluations of the reconstructed emission profiles are presented in Sec. 3. Finally, obtained results will be discussed and summarized in Sec. 4.

2. Principles

2.1 Ray-tracing setup

In this study, ray-tracing was conducted using the open source libraries Raysect and CHERAB. A three-dimensional first wall and divertor model of a 20-degree toroidal sector as in [13, 16] was used, and the 360-degree wall model was obtained by copying and rotating this sector. Same as [9–11, 13], the reflection on the wall was modeled by the Cook-Torrance micro-facet bidirectional reflectance distribution function model [17] with a single parameter of surface roughness, which defines a distribution of facets. The surface roughness parameters were set to 0.26 for beryllium (blanket modules), 0.29 for tungsten (divertor plates), and 0.13 for stainless steel (port plugs) as in [13].

A three-dimensional light source was created from a two-dimensional D_α emission profile assuming toroidal symmetry. The used emission profiles were the same as in [7] and were predicted by a combination of SOLPS-4.3 code [18, 19], which provides a coupled run of the fluid code B2 for plasma and the Monte-Carlo code Eirene for neutral particle kinetics simulation, with the OEDGE code [20], which was used to extend the SOLPS computational grid out to all plasma-facing surfaces. Table 1 summarizes the conditions used for the D_α emission calculations. Cases “d”–“o” map to shot 125501–125512 in the ITER scenario database. As can be found in [7, 13], the total D_α emission power in the scrape-off layer (SOL)

and divertor increases in the order of case from “d” to “o”, and the total power of case “l”–“o” is one order larger than case “d”–“k”. The emission profiles of case “d” and “o” are shown in Fig. 1.

Six FOVs constituting the DIM were modeled with pinhole cameras. Figures 2 shows the positions of the cam-

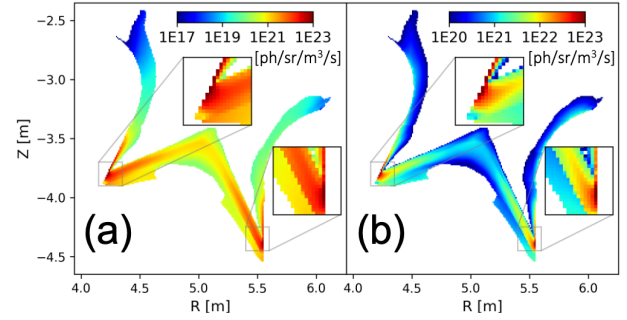


Fig. 1 The simulated D_α emission profiles of case (a) “d” and (b) “o”. Color maps are drawn in logarithmic scale.

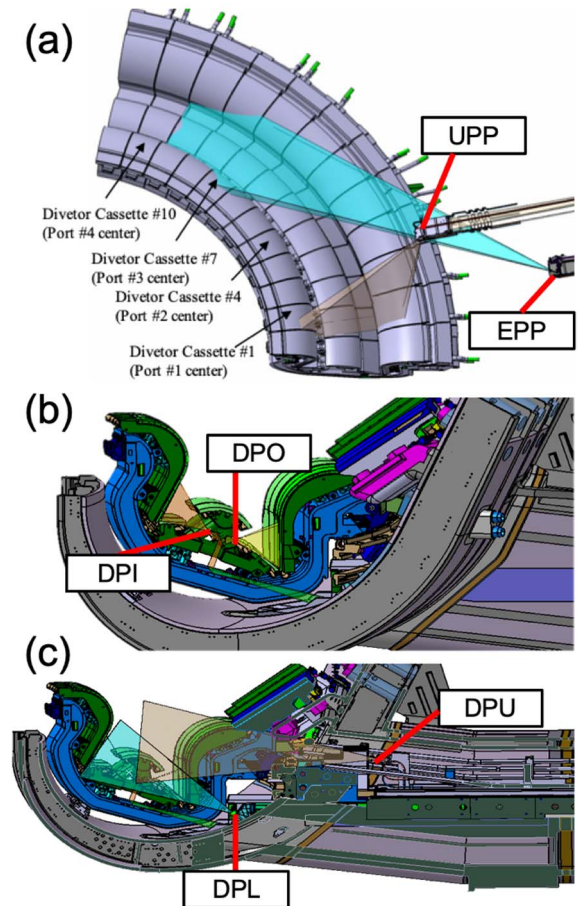


Fig. 2 The positions of pinhole cameras and their FOVs. (a) One FOV from the upper port plug (UPP), one from the equatorial port plug (EPP), (b) two in divertor port from the region under the dome for low field side (DPO) and high field side (DPI), and (c) two in the divertor port from upper position (DPU) and lower position (DPL) observing through a gap between the divertor cassettes.

Table 1 Discharge conditions d–o used for calculation [7].

Case	Pedestal /edge	Far SOL v_{perp} (ms^{-1})	Far SOL T_e (eV)	Shot (run = 2)
d	L mode	30	10	125501
e	H mode	30	10	125502
f	L mode	30	20	125503
g	H mode	30	20	125504
h	L mode	65	10	125505
i	H mode	65	10	125506
j	L mode	65	20	125507
k	H mode	65	20	125508
l	L mode	100	10	125509
m	H mode	100	10	125510
n	L mode	100	20	125511
o	H mode	100	20	125512

eras and their FOVs: one FOV from the upper port plug (UPP), one from the equatorial port plug (EPP), two in divertor port from the region under the dome for low field side (DPO) and high field side (DPI), and two in the divertor port observing through the gap between the divertor cassettes (DPU, DPL). The former two FOVs contain 71×7 aligned line-of-sights arrays, and the latter four FOVs contain 40×4 aligned line-of-sights arrays for visible light.

Usually, a ray-tracing simulation requires time-consuming runs. However, if transfer matrices, which map the relationship between emission profile and incident light on each individual receiver based on the simulation results, are once created, an additional simulation is not needed [12]. The transfer matrices were created for all receivers, and the incident light on each DIM camera was obtained by matrix multiplication as $\mathbf{g} = \mathbf{H}\mathbf{f}$, where \mathbf{g} is a vector of the measured values on the camera, \mathbf{H} is the transfer matrix, and \mathbf{f} is a vector of the emission profile. The transfer matrix will also be used in the tomography calculation as presented in the next subsection.

2.2 Computer tomography

After creating the transfer matrix, the measured signal at each camera can be calculated by matrix multiplication. Then, assuming that the measured signal and the transfer matrix are already known but the emission profile is unknown, the emission profile will be estimated. The estimation region was restricted to inside of the FOVs and within it to the region where the emission intensity exceeds 1×10^{20} ph/sr/m³/s and applied to case “o”. For inverse problem this means that the locations of the strike points and the X-point are roughly known from other diagnostics. The emission profile in the region evaluated is shown in Fig. 1. All cells in the estimated profile are squares with a side of 1 cm.

Because the transfer matrix is a singular matrix, it is not possible to obtain the emission profile as the simple calculation $\mathbf{f} = \mathbf{H}^{-1}\mathbf{g}$. To solve this ill-conditioned linear equation, we attempted four different solution methods and compared the results. The methods are the following: Tikhonov-Phillips regularization (TPR) [21], Hopfield neural network method (HNN) [22], simultaneous iterative reconstruction technique (SIRT) [23], and L-SIRT, which is the proposed method that takes logarithms of the terms used in the SIRT formula.

TPR, which is one of the most standard methods in the fusion study, minimizes $\gamma|\mathbf{C}\mathbf{f}|^2 + |\mathbf{g} - \mathbf{H}\mathbf{f}|^2$, where γ are the relaxation coefficients and \mathbf{C} is the side constraint operator. HNN is the method that adds to TPR a constraint that all reconstructed values must be positive. HNN used the skimmer function as an activation function in [20], but because the values processed here are of a very high order, an overflow occurs when evaluating the exponential term in the function. Therefore, we used the ramp function instead of the skimmer function. In this study, γ were tuned

by the L-curve method [24], and an identity matrix was used for \mathbf{C} .

SIRT method updates the solution by the following sequential calculation;

$$\mathbf{f}^{(k+1)} = \mathbf{f}^{(k)} + \alpha \mathbf{H}^T (\mathbf{g} - \mathbf{H}\mathbf{f}^{(k)}), \quad (1)$$

where k is the iteration number, and α is a relaxation coefficient. When the estimated value became negative in iterative calculations, the value is replaced with zero. Finally, L-SIRT method that takes logarithms of all terms in Eqs. (1) to consider a wider range of values, is defined as follows:

$$\log f_i^{(k+1)} = \log f_i^{(k)} + \alpha \left\{ \log(\mathbf{H}^T \mathbf{g})_i - \log(\mathbf{H}^T \mathbf{H}\mathbf{f}^{(k)})_i \right\}, \quad (2)$$

where i is the index number of the vector of the estimated emission profiles. The value α in Eqs. (1) and (2) was set to unity. Because this method estimates the logarithm of the emission intensity, the estimated emission intensity is always positive in principle.

2.3 Consideration of reflection effects and evaluation of reconstructed emission profiles

Before comparing the solutions for each of the methods applied, we present the mitigation of the reconstruction errors by applying transfer matrices that consider the reflection effects. Figure 1 (a) shows the original emission profile of case “o”. Figures 3 (a), (b) show emission profiles reconstructed by TRP with the transfer matrix not considering and considering the reflection effects, respectively. The color maps are plotted in logarithmic scale, and the regions where the values are less than zero are colored in black. To evaluate reconstructed emission profiles, we used the figure-of-merit (FOM) [25] defined as

$$\text{FOM} = \frac{\|\mathbf{f}_{\text{rec}} - \mathbf{f}_{\text{ori}}\|}{\|\mathbf{f}_{\text{ori}}\|}, \quad (3)$$

where the $\|\cdot\|$ is a calculation of norm, the \mathbf{f}_{rec} is a vector of the reconstructed profile, and the \mathbf{f}_{ori} is a vector of the original profile. The FOMs for reconstructed profiles in Figs. 3 (a), (b) are 1.7 and 0.76, respectively. Also, the fractions of the regions with negative values (η) are 43% and 20% in Figs. 3 (a), (b), respectively. With consideration of reflection effects, the FOMs became lower than without consideration of reflection effects. The regions with negative values were reduced, also the overall overestimation of positive values seen in Fig. 3 (a) was decreased.

Because the emission profiles have values in the wide range and FOM is sensitive to errors at regions where the values are large such as in strike points, we also utilized root-mean-squared-logarithmic-error (RMSLE) [26] defined as follows as an index

$$\text{RMSLE} = \sqrt{\frac{1}{2} \sum_i^n \{\log(f_{\text{rec},i} + 1) - \log(f_{\text{ori},i} + 1)\}^2}. \quad (4)$$

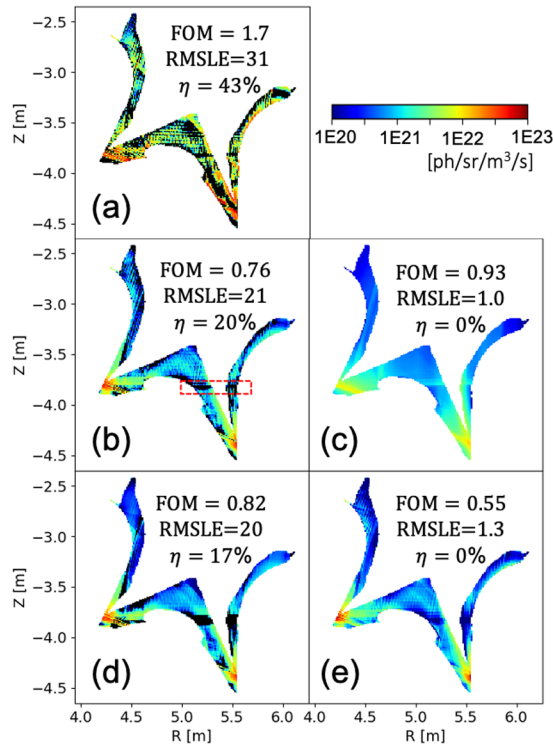


Fig. 3 Profiles reconstructed by (a), (b) TPR (c), HNN, (d) SIRT, and (e) L-SIRT, using the transfer matrices (b) not considering and (b) - (e) considering the reflection effects. Color maps are drawn in logarithmic scale and negative values are colored in black. Figure-of-merit (FOM), root-mean-squared-logarithmic-error (RMSLE), and the fraction of negative-value cells (η) are given for each case.

Because RMSLE cannot be calculated if f_{rec} contains negative values, the negative values were replaced with zero. The RMSLEs, which also reflects estimation errors from low emission intensity, for the profiles in Figs. 3 (a), (b) are 31 and 21, respectively.

The Since the effectiveness of consideration of the reflection effects in the tomography process was confirmed, the reconstructions in the following section were calculated with making use of the transfer matrices considering the reflection effects.

3. Results

3.1 Comparison of solution methods for tomography

We would begin with comparing tomography solution methods using case “o”, and Figs. 3 (c) - (e) show the emission profiles reconstructed by different other solution methods for tomography than TPR. The profile in Fig. 3 (d) was reconstructed by HNN method without negative values. The RMSLE for this profile showed 1.0, which is the smallest in the used solution methods. However, the profile looks flat and could not express the high emission regions around the strike points well. Thereby, the FOM for HNN method was 0.93, which was larger than that for TPR with

Table 2 The FOM, RMSLE and η of case “d” and “o”.

Case	Solution	FOM	RMSLE	η (%)
d	TPR	0.76	24	28
	HNN	0.93	2.5	0
	SIRT	0.82	25	32
	L-SIRT	0.54	1.6	0
o	TPR	0.76	21	20
	HNN	0.93	1.0	0
	SIRT	0.82	20	17
	L-SIRT	0.55	1.3	0

negative values.

The profile in Fig. 3 (d) was reconstructed by SIRT. The FOM, RMSLE, and η of this profile are 0.82, 20, and 17%, respectively. Although of this profile is less than that by TPR, the FOM of this profile is greater. The profile in Fig. 3 (e) was reconstructed by L-SIRT. The FOM of this profile is 0.55, which is the smallest value among the used solution methods. Although the reconstructed profile resembles that by SIRT in Fig. 3 (d), the regions with negative values have disappeared. Additionally, the RSLME for this profile is 1.3, which is the second smallest value among the used solution methods. Considering the combination of FOM and RSLME, the profile reconstructed by the L-SIRT showed the best performance and reconstructed well both the high emission at the strike points and the low emission in the other regions. The FOMs, RMSLEs, and η of case “d” and “o” are summarized in Table 2. L-SIRT showed the lowest FOM and RMSLE in case “d”. In other cases, L-SIRT also showed the most agreeable results among the four methods.

The area inside the red dotted box in Fig. 3 (b) is always underestimated in Figs. 3 except for Fig. 3 (c). This area is observed together with the inner strike point by the DPU receiver, whose line-of-sights pass through the gap between divertor cassettes. Because the emission intensity at the strike point is larger than that inside the box and the error of reconstruction at the inner strike point is also relatively large, it is likely that the area inside the box was strongly affected by the large error at the strike point. Since the area of the box is also observed by the UPP and EPP receivers, it is not a problem to mask the DPU receivers that observe this area. One of the calculation results using L-SIRT with ignoring the line-of-sights of DPU receivers that observe the area of the box and the inner strike point together is shown in Fig. 4 (a). Although the line-of-sight data for the tomography calculations was reduced and the RMSLE became slightly larger, the artificial underestimation inside the red dotted box in the emission profile disappeared and the FOM became smaller. In the calculations in the next sections, such line-of-sights of DPU were ignored.

3.2 Dependence of the reconstruction quality on the number of FOVs used

Because the components of DIM, especially for DPI

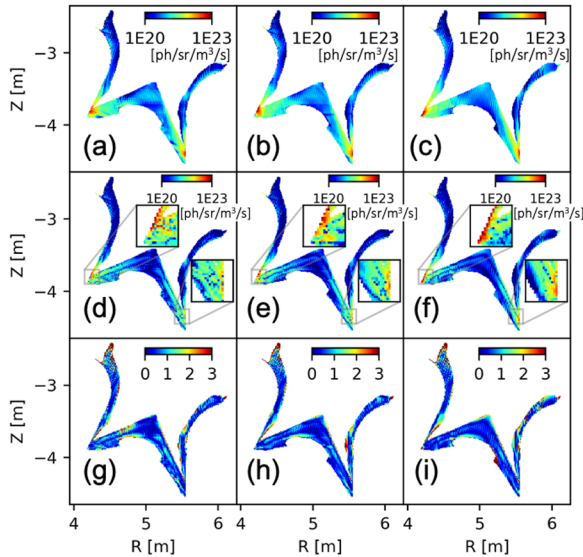


Fig. 4 (a), (b), (c) The f_{rec} , (d), (e), (f) $|f_{\text{rec}} - f_{\text{ori}}|$, and (g), (h), (i) $|\log f_{\text{rec},j} - \log f_{\text{ori},j}|$ of case “o” reconstructed by L-SIRT making use of (a), (d), (g) six FOVs, (b), (e), (h) four FOVs, and (c), (f), (i) two FOVs. Color maps are plotted in (a) - (f) logarithmic scale and (g) - (h) linear scale.

and DPO, allocated in the divertor port will be subjected to heat load from the divertor region, there is a concern that the optical components will be deformed by the heat load. Additionally, because the DPU and DPL are the FOVs through the narrow gap and require a high alignment accuracy, there is a fear of long-term performance after the installation [27]. Therefore, it is of importance to investigate the variation in the measurement performance with fewer FOVs.

Three situations with (i) all FOVs, (ii) four FOVs (UPP, EPP, DPU, DPL), and (iii) two FOVs (UPP, EPP) were investigated. Figs. 4 (a) - (c) show the emission profiles of case “o” reconstructed by L-SIRT in the (i-iii) situations, respectively. The absolute errors of each profile ($|f_{\text{rec}} - f_{\text{ori}}|$) are shown in Figs. 4 (e) - (f) in logarithmic scale. Also, the absolute errors of logarithmic differences ($|\log f_{\text{rec},i} - \log f_{\text{ori},i}|$) are shown in Figs. 4 (g) - (i) in linear scale.

The reconstructed profiles with all FOVs used and four FOVs used are similar overall. The FOMs of the profiles with all FOVs and four FOVs are 0.51 and 0.59, respectively. The slight FOM change is caused by a deterioration at the strike point because the two removed FOVs observe the high emission regions at the strike points. On the other hand, the region around the baffle is not included in the two removed FOVs. Therefore, the accuracy in the top region was not affected significantly by removing them, so that remarkable changes between in Figs. 4 (g) and (h) are not seen. The RMSLEs of the profiles with all FOVs and four FOVs are 1.5 and 1.4, respectively.

With only two FOVs, it was possible to reconstruct the profile as seen in Fig. 4 (c). However, the errors at the

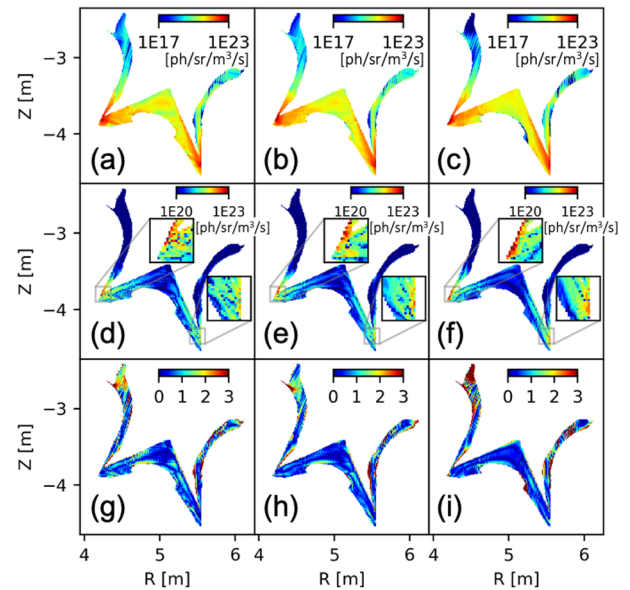


Fig. 5 (a), (b), (c) The f_{rec} , (d), (e), (f) $|f_{\text{rec}} - f_{\text{ori}}|$, and (g), (h), (i) $|\log f_{\text{rec},j} - \log f_{\text{ori},j}|$ of case “d” reconstructed by L-SIRT making use of (a), (d), (g) six FOVs, (b), (e), (h) four FOVs, and (c), (f), (i) two FOVs. Colormaps are plotted in (a) - (f) logarithmic scale and (g) - (h) linear scale.

strike points became larger than those for the profile reconstructed with four FOVs. The FOM of the profile reconstructed with two FOVs is 0.83. In this reconstructed profile, the position of the high emission area in the high field side moved downward, and the error around there is larger than that in the low field side. This is because the remained two FOVs do not include line-of-sights observing the high emission region in the high field side directly. In other words, the region was reconstructed from the reflected light, resulting in ambiguity. The logarithmic error around the baffle are slightly larger as seen in Fig. 4 (i), but the RMSLE of this profile is 1.9, which is worse than that for the four FOVs reconstruction. The increase in the logarithmic error is caused by removing the two FOVs that observe the region around the baffle. As the remaining UPP and EPP receivers also observe the region around the baffle, excessive deterioration in accuracy was prevented.

Figures 5 show the reconstructed emission profiles and errors for the case “d” in the (i-iii) situations. Similar to case “o”, the absolute errors increase with the decreasing number of FOVs used for reconstructions. The FOMs of the profiles with all FOVs, four FOVs, and two FOVs are 0.56, 0.58, and 0.82, respectively. These FOMs are almost the same as the FOMs for the case “o” in each situation. On the other hand, the logarithmic differences increased to a greater degree than in the case “o” when only two FOVs were used, especially in the region around the baffle, as seen in Fig. 5 (i). The RMSLEs of the profiles with all FOVs, four FOVs, and two FOVs are 1.6, 1.4, and 2.8, respectively. Because the emission intensity around the baffle is 6 orders of magnitude smaller than the highest

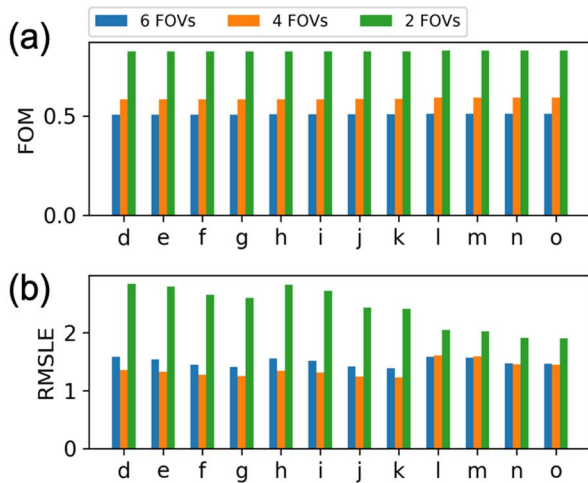


Fig. 6 Comparison of reconstruction quality for a range of discharge conditions as quantified by: (a) FOM and (b) RMSLE and considering different number of FOVs used for reconstruction of the emission profiles.

emission intensity at the strike point, it is more difficult to reconstruct, which leads to larger errors.

3.3 Evaluation among discharge conditions

We evaluated the reconstructed emission profile of all the cases from “d” to “o” by FOM and RMSLE. The profiles were reconstructed by L-SIRT while changing the number of FOVs. The results are shown in Fig. 6. With decreasing number of FOVs used, the FOMs of all cases are increased, and the increase in the FOM is significant when only two FOVs were used. Also, sizeable differences in the FOM among cases are not observed. Therefore, because the FOM reflects mostly the errors in the high emission regions at the strike points, and these are dominant in all cases, the accuracy of the reconstruction of the strike points, as quantified by this figure, does not vary significantly when the discharge condition changed.

On the other hand, RMSLE, which reflects errors from wide range of values more equally, is more dependent on the case. The RMSLEs of the cases “d” to “k” with four FOVs used are smaller than those with all FOVs used. This may be due to the use of the constant relaxation coefficient α and may be improved by using a relaxation coefficient weighted for each line-of-sight. RMSLEs of cases “l” to “o” with four FOVs are comparable. The RMSLE is larger when only two FOVs were used for reconstruction, especially in cases “d” to “k”, and decreases as the emission intensity increases. This is because the RMSLE is sensitive to the logarithmic errors in the region around the baffle, and the cases with lower emission intensity there show larger logarithmic errors, as seen in Fig. 5 (i).

4. Discussion and Summary

We have attempted the reconstruction of the emission

profile by several solution methods for tomography. The solution method which minimizes errors in logarithmic scale (L-SIRT) showed better performance than the solution methods which minimize errors in linear scale (TPR, HNN, SIRT). This is because the solution methods which minimize linear scale errors are less sensitive to errors in the regions where the emission intensity is low while the values in the emission profile vary in a wide range of orders of magnitude. As the HNN method could not reconstruct the fine details of the profile, it was not enough to impose the constraint to the TPR method that all values must be positive to get a satisfactory reconstruction. On the other hand, L-SIRT considered errors even in the region of low emission and at the same time imposes the constraint that all values are positive. Such features are compatible with DIM reconstruction calculations and make possible the reconstruction with higher accuracy.

The reconstruction was attempted by changing the number of used field-of-views (FOVs). When removing the two FOVs from under the dome (DPI, DPO), the accuracy of the reconstruction of high emission at the strike points became lower. When removing the rest of the two FOVs in the divertor port additionally, the accuracy of both of the regions at the strike points and around the baffle became much worse. Comparing the reconstruction performance for emission profiles for a range of plasma conditions it is found that, although the error at the strike point did not differ much, the errors around the baffle became severe in the cases where the range of emission values was wider. In such cases, the emission around the baffle is six orders of magnitude smaller than the highest value at strike points. Therefore, reconstruction in low power discharges that are characteristic of a wider range of emission values is more challenging with few FOVs, especially in the low emission regions.

This study was performed based on a ray-tracing approach. We have created the transfer matrices considering the reflection effects on the wall surface. The reflection modeling depends on a single parameter, roughness. As analyzed in detail in [13], the selection of the parameter roughness parameter is also important to reconstruct the emission profile accurately, while the surface roughness may change throughout the periods of ITER operation. Assuming that an in-situ determination of roughness is possible, the reconstruction of the emission profile in the divertor region could be performed as seen in this paper.

Acknowledgments

We would like to thank M. Carr, A. Meakins and all developers of Raysect and CHERAB codes. One of Authors (H.N) is grateful to Dr. M. Hosokawa, Dr. S. Pinches, and the ITER Organization for their hospitality and support during his internship in the second half of 2019. This work was partially supported by the NINS program of Promoting Research by Networking among Institutions (No.

01411702).

The views and opinions expressed herein do not necessarily reflect those of the ITER Organization.

- [1] H. Ogawa *et al.*, “Design of Impurity Influx Monitor (Divertor) for ITER” JAEA-Tech. 2006-015 (2006). <http://jolissrch-inter.tokai-sc.jaea.go.jp/pdfdata/JAEA-Technology-2006-015.pdf>
- [2] H. Ogawa *et al.*, “Research and development of optical diagnostics for ITER” Paper IT/P6-23 (2009).
- [3] H. Ogawa *et al.*, Fusion Eng. Des. **83**, 1405 (2008).
- [4] S. Kitazawa and H. Ogawa, Fusion Eng. Des. **112**, 74 (2016).
- [5] A. Iwamae *et al.*, Plasma Fusion Res. **4**, 042 (2009).
- [6] T. Sugie *et al.*, J. Plasma Fusion Res. **79**, 1051 (2003).
- [7] S. Kajita *et al.*, Plasma Phys. Control. Fusion **55**, 085020 (2013).
- [8] K.-D. Zastrow *et al.*, Rev. Sci. Instrum. **79**, 10F527 (2008).
- [9] M. Carr *et al.*, Rev. Sci. Instrum. **90**, 043504 (2019).
- [10] M. Carr *et al.*, Rev. Sci. Instrum. **89**, 083506 (2018).
- [11] J. Karhunen *et al.*, Rev. Sci. Instrum. **90**, 103504 (2019).
- [12] S. Kajita *et al.*, Contrib. Plasma Phys. **56**, No.9, 837 (2016).
- [13] V.S. Neverov *et al.*, Plasma Phys. Control. Fusion **62**, 115014 (2020).
- [14] A. Meakins and M. Carr, “Raysect Python raytracing package,” version v0.6.1, Zenodo (2020). <https://doi.org/10.5281/zenodo.3633959>
- [15] C. Giroud *et al.*, “CHERAB spectroscopy modelling framework,” Zenodo, version v1.2.0 (2019). <https://doi.org/10.5281/zenodo.3551871>
- [16] J. Romazanov *et al.*, Contrib. Plasma Phys. e201900149 (2019). <https://doi.org/10.1002/ctpp.201900149>
- [17] R.L. Cook and K.E. Torrance, ACM Trans. Graphics **1**, 7 (1982).
- [18] H.D. Pacher *et al.*, J. Nucl. Mater. **463**, 591 (2015).
- [19] R.A. Pitts *et al.*, Nucl. Mater. Energy **20**, 100696 (2019).
- [20] S.W. Ligo *et al.*, J. Nucl. Mater. **415** (1), S965 (2011).
- [21] N. Iwama *et al.*, Appl. Phys. Lett. **54**, 502 (1989).
- [22] N. Iwama *et al.*, J. Plasma Fusion Res. SERIES **8**, 0691 (2009).
- [23] G.T. Herman *et al.*, Comput. Biol. Med. **6**, 273 (1976).
- [24] P.C. Hansen *et al.*, IAM J. Sci. Comput. **14**, 1487 (1993).
- [25] A. Wingen *et al.*, J. Plasma Fusion Res. **93**, No.2, 91 (2017).
- [26] S. Jachner *et al.*, J. Stat. Softw. **22**, 1 (2007).
- [27] S. Kajita *et al.*, J. Instrum. **15**, P11035 (2020).